Article:

Labit, B., Canal, G. P., Christen, N. et al. (10 more authors) (2017) Experimental studies of the snowflake divertor in TCV. Nuclear Materials and Energy. ISSN 2352-1791

https://doi.org/10.1016/j.nme.2017.03.013

Experimental Studies of the Snowflake Divertor in TCV

B. Labit[a], G.P. Canal[a,1], N. Christen[a], B.P. Duval[a], B. Lipschultz[b], T. Lunt[c], F. Nespoli[a], H. Reimerdes[a], U. Sheikh[a], C. Theiler[a], C.K. Tsui[d,a], K. Verhaegh[b,a], W.A.J. Vijvers[e]

[a] *Swiss Plasma Center, Ecole Polytechnique Fédérale de Lausanne, Station 13, CH-1015 Lausanne, Switzerland*
[b] *York Plasma Institute, University of York, York, UK*
[c] *Max Planck Institut für Plasmaphysik, Boltzmannstr. 2, 85748 Garching, Germany*
[d] *University of California San Diego (UCSD), San Diego, CA, USA*
[e] *FOM Institute DIFFER, Nieuwegein, The Netherlands*

Abstract

To address the risk that, in a fusion reactor, the conventional single-null divertor (SND) configuration may not be able to handle the power exhaust, alternative divertor configurations, such as the Snowflake divertor (SFD), are investigated in TCV. The expected benefits of the SFD-minus in terms of power load and peak heat flux are discussed and compared to experimental measurements. In addition, key results obtained during the last years are summarized.

Keywords: tokamaks, snowflake divertor, detachment, heat load mitigation

1. Introduction

In a fusion reactor like DEMO, the power crossing the separatrix will be of the order of 150 MW. On the other hand, the divertor targets specifications require the peak heat flux to be below 10 MW.m^{-2} in order to avoid melting and also to reduce T_i below 5 eV to avoid excessive sputtering. To satisfy those constrains, one has to increase the target wetted area and to operate with a radiated power fraction $f_{rad} > 90\%$ and a detached divertor. At the same time, the detachment must be robust and the core confinement must be acceptable. To address the risk that the conventional single-null divertor (SND) may not be able to handle the power exhaust, alternative divertor geometries, namely the Snowflake Divertor [1], the X-Divertor [2], the Super-X Divertor [3] and the X-Point Target Divertor [4] are currently under investigation in TCV.

The Snowflake divertor (SFD) is a second-order null configuration where not only the magnetic poloidal field B_p vanishes in the null region but also its spatial derivative ∇B_p. Such configuration splits the separatrix near the null into six segments: two enclose the confined plasma and four lead to the machine wall (the divertor legs). The SFD configuration also results in a longer connection length and in a larger divertor volume, which may lead to higher radiated power losses in the SOL and so facilitate plasma detachment. Moreover the low poloidal magnetic field may lead to enhanced cross-field transport, which would increase the wetted area. However, the SFD requires more divertor coils and higher divertor coil currents, which might be a serious limitation for fusion reactors. In practice, the exact SFD can only be approximated by a configuration with two nearby X-points, defining primary and secondary separatrices and their associated strike points. If the secondary X-point is located in the private flux region, the SFD is refered to as SF+ while if it located in the common flux region, it is referred to as SF-.

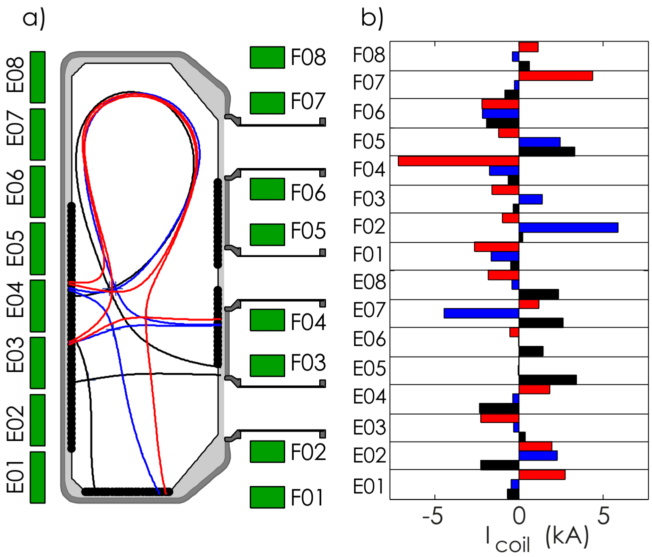

Figure 1: a) TCV cross section with the 16 poloidal field coils (green) and the wall embedded Langmuir probes (black dots). For shot #48133, separatrices for SND (black, t = 0.4 s), SF+ (blue, t = 0.8 s) and SF- (red, t = 1.4 s); b) Current in the poloidal field coils for the 3 divertor configurations. The current limit is 7.7 kA.

2. Experimental setup and diagnostics

TCV is a medium size tokamak with nominal parameters R = 0.88 m, B_T < 1.5 T, I_p < 1 MA [5]. Figure 1a) rep-

[1] Present address: General Atomics, San Diego, California 92186-5608, USA

resents the TCV poloidal cross-section with the 16 independently powered PF coils. This allows an extreme flexibility in the core plasma shape with a large variety of shaping parameters: $-0.6 \leq \delta \leq +0.6$, $1 \leq \kappa \leq 2.8$ and in divertor configurations. The experimental feasibility of the snowflake divertor was demonstrated for the first time in TCV [6]. An illustration of this flexibility is shown in Fig1a) where three different divertor configurations: SND, SF+ and SF- were achieved within the same shot. For this shot, the current feeding the shaping coils was varied as shown in Fig.1b). In Fig2, some SOL properties are compared between SND, SF+ and SF-. Since TCV features a wide open divertor, the strike points on the wall are relatively far from the null region so that the flux expansion is usually strongly reduced at the targets compared to the null region. Thus, the expected benefits of the SF+ compared to the SND are only expected in the immediate vicinity of the last closed flux surface (LCFS) while for the SF-, the advantages cover a large fraction of the SOL with a typically characteristic power fall of length evaluated at the outboard midplane of $\lambda_{q,u} \sim 8\,\mathrm{mm}$.

TCV is equipped with 114 wall embedded Langmuir probes (Fig.1a)), which cover about 65% of the graphite wall poloidal circumference. This allows to measure plasma parameters at all the strike points (note that currently only 48 amplifiers are available). The I-V characteristics is fitted with a 4-parameter fit and the minimum fitted temperature is returned [7]. The heat load along the target coordinate s is estimated from the relationship $q_{\perp}(s) = J_{sat,\perp}(s)\left(\gamma T_e(s) + \epsilon_{pot}\right)$ where the value of the sheath heat transmission factor γ=5 based on previous experiments on TCV [8] and ϵ_{pot} is the potential energy per incident ion that includes the ionization potential of 13.6 eV and half of the molecular binding energy, which is 2.2 eV. The heat load is also measured with infrared thermography. Two infrared cameras are installed on TCV, one imaging the vessel floor from the machine roof, the other imaging the inner wall from the low field side [9]. The heat flux is computed from the measured tile temperature with the code THEODOR [10]. Radiated power is measured by 64 gold foil bolometers allowing for tomographic inversions and complemented with 140 AXUV photodiodes. Additional spectroscopic divertor diagnostics have been recently installed to measure the visible-UV spectrum [11] and/or specific spectral lines [12].

3. Power exhaust and radiation limit in SF+ configuration

Even though in TCV, the expected benefits of the SF+ are limited only to a narrow region of the SOL in the vicinity of the separatrix, significant changes of the plasma behavior have been observed when the divertor configuration is varied from the SND to the SF+ divertor configuration.

3.1. Evidence for enhanced cross-field transport in SF+

For L-mode attached plasmas, measurements in the SF+ show that the ratio of the power load on the secondary strike points to the power load on the primary strike points increases up to 10% when the distance separating both X-points is decreased [13]. A comparison with EMC3-Eirene simulations

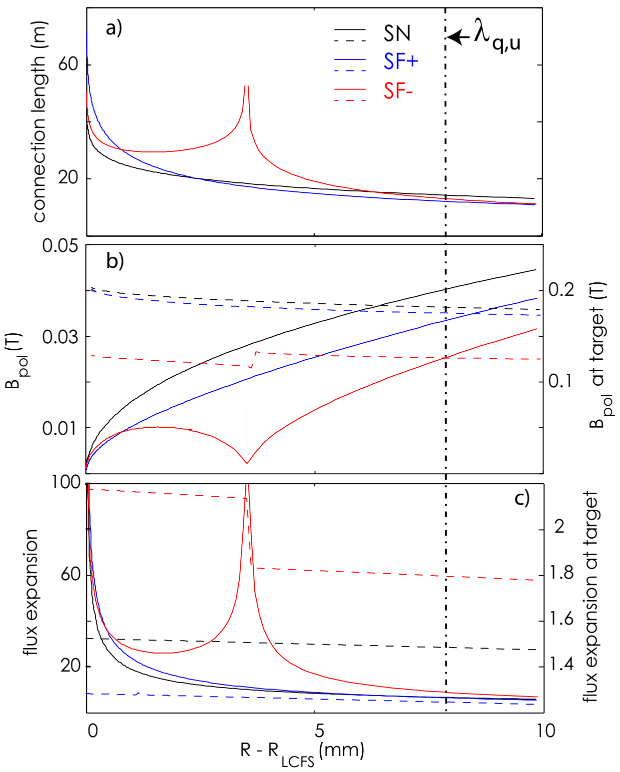

Figure 2: a) Scrape-Off Layer properties for shot #48133, for SND (black, $t = 0.4\,s$), SF+ (blue, $t = 0.8\,s$) and SF- (red, $t = 1.4\,s$): a) connection length from outboard midplane to outer target (solid); b) Minimum poloidal magnetic field B_θ (solid) and poloidal magnetic field at the outer target (dashed); c) Flux expansion at minimum B_θ (solid) and flux expansion at outer target (dashed). The y-axis for dashed curves is on the right.

[14] shows that this cross-field transport cannot be described by the change in the field line geometry while keeping transport coefficients constant and that an additional transport channel in the null-point region has to be invoked. In Ref.[15], it is qualitatively demonstrated that the transport due to the $\vec{E} \times \vec{B}$ drift velocity can explain the measured target profiles, in particular their shape, their dependence on plasma density and on the toroidal magnetic field direction. EMC3-Eirene simulations of the SF+ [14] show that poloidal gradients of the kinetic profiles in the null-point region are larger for the SF+ than for the SND. These gradients generate a poloidal electric field in the null-point region. $\vec{E} \times \vec{B}$ particle and heat fluxes estimated *a posteriori* and not self-consistently are found to be of the same order of magnitude of the fluxes calculated by EMC3-Eirene, especially for the SF+ configuration [15]. For three different divertor configurations, the density profiles from Langmuir probes measurements at the inner strike point together with the particle source associated with $\vec{E} \times \vec{B}$ drift velocity $S_p^{\vec{E}\times\vec{B}} = \nabla \cdot \Gamma_p^{\vec{E}\times\vec{B}}$ are shown in Fig.3. To further quantify the importance of cross-field transport, numerical simulations this time with self-consistent $\vec{E} \times \vec{B}$ flows of the SF+ configuration have been initiated using the UEDGE code [16].

For ELMy H-mode, the power repartition to secondary strike

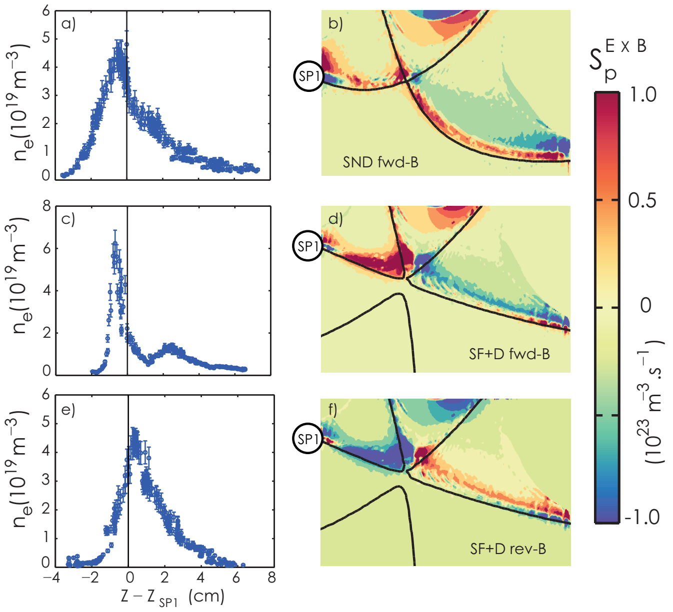

Figure 3: Density profiles measured with Langmuir probes at SP1 (left) and particle source $S_p^{E\times B}$ computed from EMC3 simulations (right) for SN fwd-B (a-b), SF+ fwd-B (c-d), SF+ rev-B (e-f).

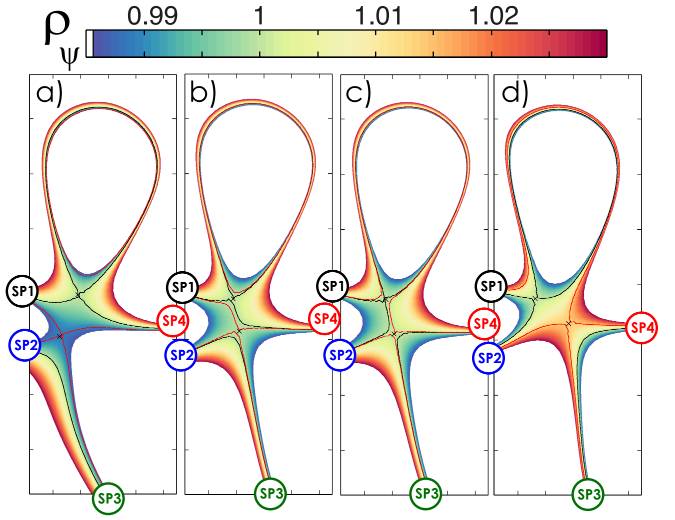

Figure 4: Maps of ρ_ψ for a TCV shot (#48133) with a transition from SF+ to SF- (LFS). The primary separatrix is shown in black, the secondary one in red. The normalized distance between X-points is $\rho_{\psi,X2}$=0.9889 a), 0.9990 b), 1.0007 c) and 1.0143 d).

points is further enhanced (reaching up to 40%) and indicates that SFD advantages may be particularly strong in the challenging situation of high heat fluxes as encountered during ELMs [17]. Several mechanisms for future investigations can be invoked to explain this observation: a transitory change from SF+ to SF- induced by the ELM currents, β-induced instabilities [18] or an enhanced $\vec{E} \times \vec{B}$ transport.

3.2. *Detachment and radiation limit in the SF+ configuration*

Any viable power exhaust solution for fusion reactors will likely rely on plasmas detached from the targets and on a large fraction of radiated power in the SOL. The accessibility to plasma detachment for SF+ has been investigated either by increasing the density or by seeding neon impurity in the private flux region, and compared to the SND [20]. In TCV, the radiation is usually due to the ubiquitous carbon impurities in the carbon-tile covered vessel. The plasma density, and, therefore, the carbon density, was varied from $\langle n_e \rangle = 2.5 \times 10^{19} m^{-3}$ to $10 \times 10^{19} m^{-3}$. The increase of $\langle n_e \rangle$ results in an increase of the radiated power $P_{\rm rad}$, an increase of the ohmic heating power $P_{\rm Ohm}$ and an increase of the radiated power fraction, $f_{\rm rad} = P_{\rm rad}/P_{\rm Ohm}$ from 30% to about 65%, for both configurations. Nevertheless, the SF+ configuration radiates up to 10% less power than the SND configuration at large densities.

The impurity seeding experiments were performed using neon puffs in discharges with a low density of $\langle n_e \rangle \simeq 2.5 \times 10^{19}\ {\rm m}^{-3}$. The integrated, uncalibrated neon flux measurements lead to similar increases of $Z_{\rm eff}$ from approximately 1.8 to 6 for both configurations, indicating a similar penetration of neon into the confined plasma. When increasing the neon content, both $P_{\rm rad}$ and $P_{\rm Ohm}$ increase, resulting in an increase of $f_{\rm rad}$ from 30% to 70%. For the same value of $Z_{\rm eff}$, strong neon seeding leads up to 15% more radiation in the SF+ configuration than in the SND configuration. This is opposite to the geometry dependence with increasing $\langle n_e \rangle$ and might be explained by the temperature dependence of the neon radiative loss parameter (peaking at $T_e \simeq 40\,{\rm eV}$), which significantly differs from that of carbon (peaking at $T_e < 10\,{\rm eV}$). For both cases, the radiation region in the SND remains close to the inner target while in the SF+, the radiation region is significantly larger, extending past the null region further upstream.

In both cases, and for both divertor configurations, an increase in $f_{\rm rad}$ is accompanied by a decrease of the power distribution to the inner strike points and a broadening of the heat flux profile at the target. In addition, at large $f_{\rm rad}$, the inner targets show signs of the onset of detachment while the outer divertor remains fully attached.

A common limitation in both configurations is that the core fraction of the radiation, $f_{\rm core} = P_{\rm rad,core}/P_{\rm rad}$, increases similarly with $f_{\rm rad}$. In these experiments $f_{\rm rad}$ and, hence, access to full detachment was limited at approximately 60% of the Greenwald density by the onset of a long-wavelength MHD instability and not by a radiation instability, seen as the ultimate limit of radiative divertor performance.

The physics of the plasma detachment is also investigated for the SND configuration [11, 12] and for other alternative divertors [21], revealing high levels of detachment of the outer strike point and geometrical dependencies in rev-B discharges.

4. Heat load optimization in the SF- divertor

4.1. Simple modelling of the power repartition between active strike points

The SF- configuration is topologicaly different than the SF+ configuration since one side of the SOL is split by the secondary X-point and, therefore, a secondary strike point is activated on this SOL side in addition to the primary one. It is convenient to introduce the normalized poloidal flux $\rho_\psi \equiv \sqrt{\frac{\psi-\psi_0}{\psi_{X1}-\psi_0}}$ as a radial coordinate, with ψ being the poloidal flux and ψ_0 and ψ_{X1} its value at the magnetic axis and at the primary X-point, respectively. In addition, in Ref [22], it was proposed to parametrize the SFD configuration by the normalized distance between the X-points defined as $\rho_{\psi,X2} \equiv \sqrt{\frac{\psi_{X2}-\psi_0}{\psi_{X1}-\psi_0}}$. SF+ configurations are characterized by $\rho_{\psi,X2} \lesssim 1$ and SF- configurations are characterized by $\rho_{\psi,X2} > 1$. Examples of TCV equilibria obtained during a transition from SF+ to SF- LFS in the same shot are shown in Fig.4. One can see how the strike point SP2 changes from secondary (SF+) to primary (SF-) and how the fraction of the upstream SOL arriving to strike point SP2 increases with $\rho_{\psi,X2}$.

In the following, the power repartition between active strike points is investigated. For this, we assume an outboard midplane profile of the form $q_\parallel(\rho_\psi) = q_0 \exp\left(\frac{\rho_\psi-\rho_{\psi,X1}}{\lambda_{\psi,u}}\right)$ where $\lambda_{\psi,u}$ is the normalized heat flux decay length. For now, let's assume that heat transport is purely parallel to the magnetic field. If the secondary X-point is located in the private flux region (SF+), the secondary strike points will not experience any heat loads since they are not connected to the upstream SOL. The entire heat load is shared by the primary strike points. Conversely, if the secondary X-point is located in the SOL (SF-), the upstream profile will be split at $\rho_{\psi,X2}$ in two parts and two active strike points (one primary, one secondary) on one side of the SOL will receive power (blue line in Fig.6b-c)).

Since the two variants of the SF- (HFS and LFS) are equivalent from the magnetic topology point of view, we will focus the discussion on the SF- LFS but the obtained results are the same for the SF- HFS with the *inner* strike points being SP3 (primary) and SP1 (secondary). For the SF- LFS, the *outer* strike points are SP2 (primary) and SP4 (secondary). The power fraction f_{SPi} $(i = 2, 4)$ is estimated as a function of $\rho_{\psi,X2}$ for various $\lambda_{\psi,u}$. This quantity is defined by the total power arriving at one strike point, normalized to the total power at both strike points: $f_{SPi} = \frac{P_{SPi}}{P_{SP2}+P_{SP4}}$ with $P_{SP2} = \int_0^{\rho_{\psi,X2}} q_{\parallel,i}(\rho_\psi) d\rho_\psi$ and $P_{SP4} = \int_{\rho_{\psi,X2}}^{+\infty} q_{\parallel,i}(\rho_\psi) d\rho_\psi$. This is illustrated on Fig. 5a) for two different upstream SOL widths $\lambda_{\psi,u}$. As expected, an optimal $\rho_{\psi,X2}$ to balance the heat loads between SP2 and SP4 can be found. Figure 5b) shows the evolution of the optimal $\rho_{\psi,X2}$ as a function of the upstream SOL width. It is important to note that, under the assumption of pure parallel transport, the peak parallel heat flux $q^{peak}_{\parallel,i}$ cannot be in balance with $\rho_{\psi,X2}$ between SP2 and SP4: $q^{peak}_{\parallel,SP2} = q_0$ for any $\rho_{\psi,X2}$.

Actually, the assumption of pure parallel transport can be relaxed by modelling the diffusion across the divertor legs. The convolution of the exponential profile with a gaussian of width

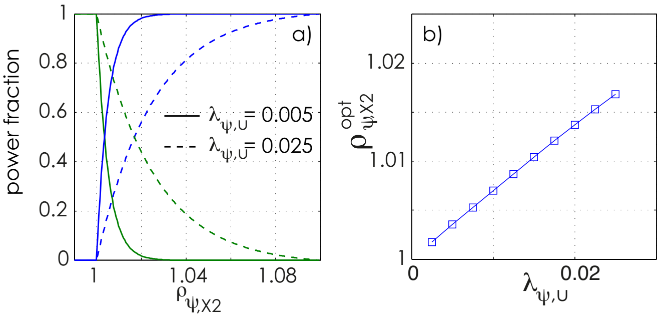

Figure 5: a) Power fraction between SP2 (blue) and SP4 (green) for two values of upstream SOL width $\lambda_{\psi,u}$. b) Optimal distance between both X-points as a function of the upstream SOL width.

S is successfully used for SND to account for diffusive spreading [23]. Here, we extend this approach to the SFD, Fig.6a-c)). The effect of the diffusive spreading in the divertor on the peak heat flux $q^{peak}_{\parallel,SP2}$ and $q^{peak}_{\parallel,SP4}$ is investigated with a scan in the parameter S for a given exponential profile, Fig.6d). Note that for a better comparison with experiments, the peak heat flux is normalised to $P_{SP2} + P_{SP4}$ with power as defined above. Indeed, the target power fraction f_{SPi} doesn't depend on S so the optimal $\rho_{\psi,X2}$ for power load balance is the same for any S. Conversely, the strength of diffusive transport has a significant effect on $q^{peak}_{\parallel,i}$: for the SF+ case, which in this context is identical to a SND, $q^{peak}_{\parallel,SP2} = 0$ and the larger is S, the lower is $q^{peak}_{\parallel,SP4}$. For the SF- case, we first see that $q^{peak}_{\parallel,SP2}$ is actually lower than $q^{peak}_{\parallel,SP4}$ for SF+ for the same S value. In addition, as for the power, the peak heat flux can be balanced between SP2 and SP4. Moreover the optimal $\rho_{\psi,X2}$ depends on the parameter S, Fig.6e). For SND plasmas, it is experimentally found that $S \leq \lambda_{\psi,u}$, so the peak heat flux is balanced at a lower $\rho_{\psi,X2}$ than for the power balance according to this modelling.

4.2. Experiments in TCV

In TCV, a $\rho_{\psi,X2}$ scan on a shot-to-shot basis in ohmic L-mode attached plasmas ($I_p \simeq 230$ kA, $n_{el} = 2.4 \times 10^{19} m^{-3}$) was performed. Both LFS SF- and HFS SF- have been explored, nevertheless, since the primary X-point is relatively close to the inner wall, the achieved $\rho_{\psi,X2}$ range is narrower for the SF- HFS case than for the SF- LFS configuration. Heat flux at the four strike points were estimated from Langmuir probes and target profiles spatial resolution was increased with strike point sweeping during steady state conditions. The profiles are fitted with the convolution of an exponential and a gaussian profiles [23]. From the fit, the power and peak heat flux values are extracted at each strike point.

To compare with the above modelling, the power fraction and the normalized peak heat flux are estimated for the two activated strike points on the split SOL side of the SF- configuration: SP1 and SP3 for SF- HFS, SP2 and SP4 for SF- LFS (squares in Fig.7). For the SF- LFS case, the power fraction and the peak heat flux can be balanced which is a clear demonstration of the benefits of the SF- configuration with respect to the

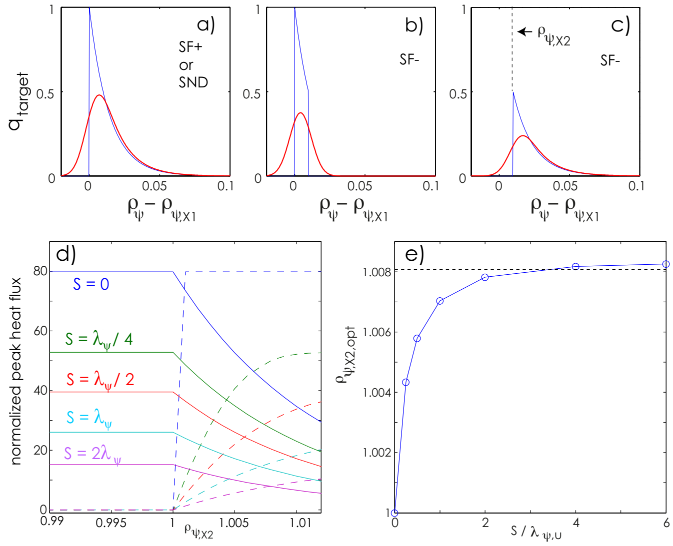

Figure 6: Heat flux profile (red) from the convolution of an exponential profile (blue) of width $\lambda_{\psi,u} = 0.012$ and a gaussian of width $S = \lambda_{\psi,u}/2$: a) at the primary strike point of a SF+ or SND. b) at one primary strike point of a SF- configuration. c) at one secondary strike point of a SF-. d) Normalized peak heat flux as a function of $\rho_{\psi,X2}$ for various S for SP4 (solid) and SP2 (dashed). d) Optimal $\rho_{\psi,X2}$ to balance $q_{\parallel}^{peak}$ (solid) and power load (dashed) as a function of S.

SF+ and SND. In addition, the optimal $\rho_{\psi,X2}$ for the power load balance is in good agreement with the expected value modelled with $\lambda_{\psi,u} = 0.012$, which corresponds to $\lambda_{q,u} = 3.6$ mm (value obtained from the target profile at SP1 in the SF+ case). For the normalized peak heat flux at SP2 and SP4, the modelling reproduces the experimental values with the same heat flux decay length ($\lambda_{\psi,u} = 0.012$) but with a different S parameter: for SP2, $S = \lambda_{\psi,u}$ and for SP4, $S = 5\lambda_{\psi,u}$. These values for S are larger than those reported for SND L-mode plasmas in TCV [24]. Understanding this difference will be subject of future work. For the SF- HFS case, the power fraction and the normalized peak heat flux are balanced for $\rho_{\psi,X2} \simeq 1.001$. This optimal distance is much shorter than the one modelled with $\lambda_{\psi,u} = 0.012$ and $S = 3\lambda_{\psi,u}$, which might be indicative of enhanced cross-field transport. This will be investigated in future work.

Finally, the possibility to balance the power load and the peak heat flux in the SF- configuration has been demonstrated through numerical simulations carried out with the EMC3-Eirene code [22].

5. Conclusion and outlook

Key results of the physics of the snowflake divertor configuration in TCV have been summarized. In addition, some expected advantages of the SF- configuration to optimize the heat loads on one side of the SOL have been demonstrated with analytical modeling. For the first time,

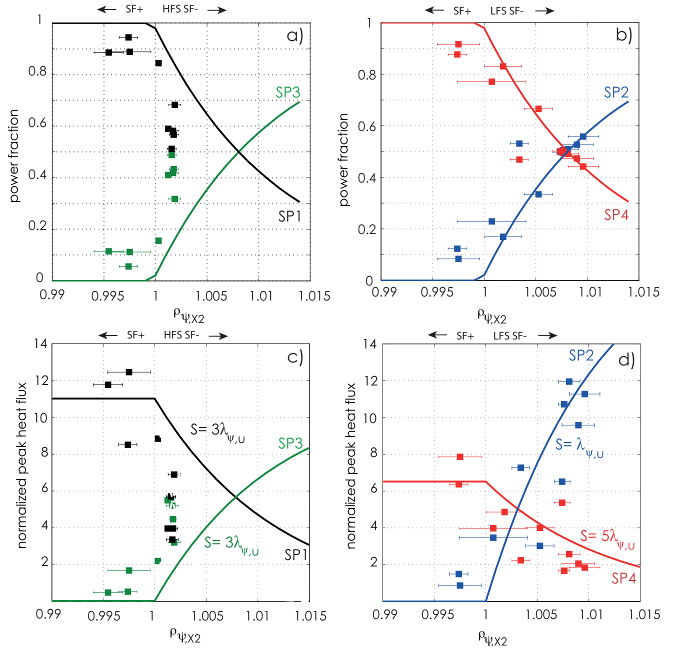

Figure 7: Comparison between experimental results (squares) and modelling (solid lines). a-b) Power fraction between active strike points on one side of the SOL: SP1 (black) and SP3 (green) for HFS SF- a); SP2 (blue) and SP4 (red) for LFS SF- b); c-d) Normalized peak heat flux between active strike points on one side of the SOL: c) SP1 and SP3 for HFS SF-; d) SP2 and SP4 for LFS SF-. The solid lines are the modelled power fraction and normalized peak heat flux for $\lambda_{\psi,u} = 0.012$ and different S values.

those benefits are confirmed experimentally from target heat loads measured with Langmuir probes which are also inline with simulations [22]. Following the simulations predictions, radiation limits will need to be investigated for the SF-LFS plasmas. Numerical simulations including self-consistent $E \times B$ transport but *ad hoc* turbulent transport will be continued. Finally, TCV is planning a major divertor and heating upgrade including the installation of baffles to control the divertor closure [25]. Closing the divertor aims at increasing the neutral pressure in the divertor region compared to the main chamber and improving the confinement of impurities in the divertor. The new TCV divertor will allow for increased dissipation in the divertor, while limiting detrimental effects on core performance.

[1] D.D. Ryutov Phys. Plasmas 14 (2007) 064502
[2] M. Kotschenreuther et al., Phys. Plasmas 14 (2007) 72502
[3] P. Valanju, Phys. Plasmas 16 (2009) 056110
[4] B. LaBombard et al., Nucl. Fusion 55 (2015) 053020
[5] S. Coda, Nucl. Fus., 55, (2015) 10
[6] F. Piras et al., Plasma Phys. Control. Fusion 51 (2009) 055009
[7] C. Theiler, PhD thesis, EPFL, number 5228 (2011)
[8] J. Marki et al., Journal of Nuclear Materials, 363 (2207) 382-388.
[9] R. Maurizio et al., EPS conference, Liuwen, Belgium
[10] A. Herrmann et al., Cont. Fus. Plasma Phys: Proc. 28th EPS, Funchal, ECA Vol. 25A, 2001
[11] K. Verhaegh et al., *accepted for publication in Nuclear Materials and Energy*
[12] J.R. Harrison et al., *accepted for publication in Nuclear Materials and*

Energy
[13] H. Reimerdes et al., Plasma Phys. Control. Fusion 55 (2013) 124027
[14] T. Lunt et al., Plasma Phys. Control. Fusion 56 (2014) 035009
[15] G.P. Canal et al., Nucl. Fusion 55 (2015) 123023
[16] T. D. Rognlien et al., Phys. Plasmas 6, 1851 (1999);
[17] W.A.J. Vijvers et al., Nucl. Fusion 54 (2014) 023009
[18] D.D. Ryutov et al., Physica Scripta 89 (2014) 088002
[19] R.A. Pitts et al., Journal of Nuclear Materials 290-293 (2001) 940-946
[20] H. Reimerdes et al., Journal of Nuclear Materials, 463 (2015) 1196-1199
[21] C. Theiler et al., ”Results from recent detachment experiments in alternative divertor configurations on TCV”, submitted to Nucl. Fusion
[22] T. Lunt et al., Plasma Phys. Control. Fusion 58 (2016) 045027
[23] T. Eich et al., Phys. Rev. Lett. 107, (2011) 215001
[24] A. Gallo et al., *accepted for publication in Nuclear Materials and Energy*
[25] H. Reimerdes et al., *this conference*